Journal of Nonlinear and Convex Analysis
Volume 26, Number 7, 2025, 2375–2389

Yokohama Publishers
ISSN 1880-5221 ONLINE JOURNAL

PULSE WAVE MORPHOLOGICAL FEATURE CLASSIFICATION AND TIME DOMAIN FEATURE RECOGNITION METHOD BASED ON 1D-DCNN MODEL

YANG LI*, XINGGUANG GENG†, FEI YAO, HAO WANG, YITAO ZHANG†, XIAOYU WANG§, AND HUA HUA

Abstract. Pulse wave time-domain characteristics are essential for blood pressure monitoring and cardiovascular disease prediction. The coordinate positions of pulse wave morphology and time-domain characteristics are closely related. Therefore, this paper proposes a time-domain feature recognition method based on morphological features for pulse waves. A three-channel pulse wave acquisition device collected radial artery pulse signals from 150 subjects. We preprocessed the signal to obtain a single-cycle pulse waveform. The next task was to identify the extreme, inflection points, and feature fusion forms of dicrotic and TWs, then classify nine pulse wave types. Finally, based on the classification characteristics of tidal and DWs, the extreme value or curvature method was used to identify the characteristic parameters of nine classes of pulse waves. To this end, we adopted a 1D-DCNN model, containing input, convolutional, fully connected, and output layers. The convolutional layer included three operation steps: convolution, activation, and max pooling. The model provided input of one-dimensional single-cycle signal data, performed convolution operations on the input data, and used the sliding of convolution kernels to capture local patterns in the input data. The activation function introduced non-linear properties into the results of convolution operations, better fitting complex data patterns. The experiment validated excellent recognition accuracy of the algorithm: 93% for DWs and 94% for TWs. This study's time-domain feature extraction algorithm for pulse waves has a minimum correction regression coefficient of 0.97 for the three types of TWs and a minimum correction coefficient of 0.96 for DWs. Corresponding to each feature point dataset, the statistical parameter values were less than 2, proving that the algorithm has achieved excellent accuracy.

1. Introduction

Pulse wave time-domain features identify the physical features of related blood flow, an important physical quantity for blood pressure estimation [4, 7, 9, 11, 18]. The simple, noninvasive, and easily obtainable features of pulse waves meet the requirements of modern continuity detection [3, 12, 13]. Accurately extracting the

2020 *Mathematics Subject Classification.* 92C55.94A08.

Key words and phrases. Pulse waves,time-domain characteristics, morphological features, the extreme point, inflection point, feature fusion.

Special Project of Sichuan Provincial Administration of Traditional Chinese Medicine(No.2023zd013). Development and Application of AI-Assisted Diagnosis and Treatment Platform Based on Zhang Zhongjing's Symptom-Pathogenesis Differentiation and Treatment. No.231111310300.

†§Corresponding author.

*†Co-first authors.

time-domain features of pulse waves is the foundation of blood pressure modeling [8, 14, 15, 20]. A complete pulse wave mainly comprises a main wave (MW), dicrotic wave (DW), and tidal wave (TW). Currently, time-domain feature parameter extraction methods mainly include the slope method (SM), slope and threshold combination method (STCM), differential method (DM), wavelet method (WM), etc. The SM and STCM are achieved through the abrupt change of the slope of the pulse wave at the feature point to achieve feature recognition [21]. The DM mainly achieves feature recognition by differentiating the waveform and finding the zero point position of the pulse wave characteristics. They mainly use continuous wavelet decomposition to highlight pulse wave feature points at different decomposition layers and achieve wavelet transform [10, 16]. The above methods perform well in identifying pulse wave features but are susceptible to noise interference, which can lead to a decrease in recognition rate [6]. Qian et al. [19] and Chang et al. [1] proposed fitting pulse waves with three and four Gaussian functions, respectively, and calculating time-domain parameters through the parameters of the Gaussian functions. On this basis, Chen [2] used mixed genetics to fit three Gaussian functions to the pulse wave. In comparison, Sun et al. [19] applied a pulse wave model containing three Gaussian functions to generate pulse wave simulation data and used it for algorithm validation. The waveforms fitted by these models are indeed similar to real pulse waves, but their physiological significance still needs to be clarified. Whether their relevant parameters can truly represent the information in the pulse map has yet to be thoroughly studied, and there are many unknown parameters in the models, making the fitting method more complex and, therefore, less applied. Hou et al. [17] proposed a pulse wave time-domain feature recognition algorithm based on the angle method. By changing the angle, the time-domain features are obtained. This algorithm is similar to the curvature method. Wang et al. [5] proposed a pulse wave time-domain feature recognition algorithm based on deep learning algorithms. They first divided the pulse waves into six categories and used six deep-learning algorithms to classify and recognize the six types of pulse waves. However, the recognition waveform of this algorithm is limited and cannot meet the needs of practical applications. The fundamental driving force of human blood circulation comes from the periodic pumping of blood by the heart, and the ventricles mainly complete the pumping function. The activity of left ventricular contraction and relaxation forms the cardiac cycle. Left ventricular contraction injects blood into arterial blood vessels, while left ventricular relaxation draws blood into the ventricle, forming a cycle of pulse waves during this process. During the systolic phase of the heart, blood flows from the heart to the arterial ducts, causing rapid dilation of the arterial wall and the formation of the ascending branch of the MW. The height of the ascending branch mainly reflects the left ventricular ejection capacity and the compliance of the aortic vessel wall. The higher and steeper the ascending branch, the stronger the ejection capacity of the human heart and the greater the vessel wall compliance. Conversely, the weaker the ejection capacity, the smaller the vessel wall compliance. Due to the flow of blood in the tube, the pressure on the blood vessel wall decreases, forming descending branches. The external resistance causes the wave to propagate towards the near center and superimpose

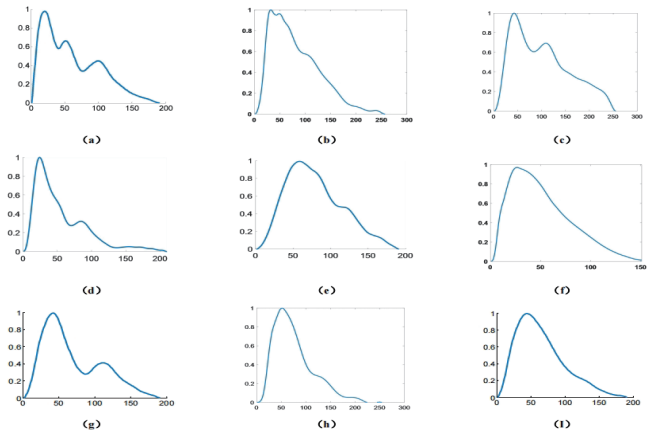

FIGURE 1. (a) Class A pulse wave (b) Class B pulse wave (c) Class C pulse wave (d) Class D pulse wave (e) Class E pulse wave (f) Class F pulse wave (g) Class G pulse wave (h) H-class pulse wave (i) I-class pulse wave

the descending branch of the MW to become a TW. TWs mainly reflect the compliance of arterial blood vessel walls. When the compliance is small, an increase in the Young modulus can lead to a high propagation rate of pulse waves, resulting in a higher amplitude of TWs, forward phase shift, and even overlapping with the MW peak. During diastole, the indoor pressure rapidly decreases, and blood within the aortic vessels begins to flow back, causing the vessel wall to retract and rapidly closing the aortic valve.As a result, a notch is formed on the pulse waveform, known as the descending isthmus (the DW trough). Due to the obstruction of the closed aortic valve, the refluxed blood flows back to the aortic canal, forming an upward wave after the descending isthmus, known as a pulsation wave, which mainly reflects the elasticity of the large artery. The increase in vascular sclerosis can lead to an increase in the conduction velocity of pulse waves, which in turn accelerates the speed of blood return and causes the phase of the DW to shift forward, even overlapping with the DW's MW peak or the front wave. A decrease in the E-value will cause a reduction in the conduction velocity of the pulse wave, increasing the velocity of blood reflux. This will cause the phase of the DW to shift backward, the descending isthmus to decrease, and the peak value of the DW to increase. From Figure 1, it can be seen that the characteristic form of the MW can be reduced to one state, namely extremum point. Tidal and DW characteristic forms can be divided into extreme points, inflection points, and feature fusion. Combining the three states of DWs and TWs, pulse waves can be divided into nine classes.

2. MATERIALS AND METHODS

2.1. **A signal acquisition instrument.** As shown in Fig. 2(a), this study uses the pulse wave acquisition device. This instrument's three compound pressure sensors can achieve synchronous pressure acquisition of three-channel signals through airbag pressurization. The pressure range is 10-140 mmHg, the pressure gradient is 20

mmHg, the sampling frequency is 225 Hz, and the pulse wavelength collected at each pressure gradient is about 2250 points. Figure 2 (b) shows a compound pressure sensor.

2.2. **Methods.** As shown in Figure 3, this method includes three parts: (i) Signal preprocessing, (ii) Classification method for nine pulse waves, and (iii) Time domain feature recognition for nine pulse waves.

2.2.1. *Data preprocessing.* Preprocessing mainly includes noise treatment, cycle division, and standardization treatment. Figure 4 shows a signal preprocessing flowchart. As shown in Figure 5 (a), because the pulse signal is a weak physiological signal on the body surface, the data acquisition equipment used in this study is a pressure sensor based on PVDF piezoelectric film. Hence, the collected data will inevitably be interfered with. Therefore, it is necessary to preprocess the collected original signal to obtain the single-cycle pulse wave in the whole period The noise carried by pulse waves mainly comprises tip, power frequency, EMG, and respiratory noise. Firstly, the median filter removes the data transient, and the 50Hz power frequency interference is removed based on the notch filter. The band-pass filter removes part of the respiratory and out-of-band EMG noises, and the new threshold function denoising algorithm based on the translation wavelet transform removes the EMG noise. Figure 5 (b) shows the denoised pulse wave sequence. The period division is mainly divided into four parts. Firstly, the Viola integral and Shannon energy algorithm extract the pulse signal's envelope energy function. Secondly, the optimal peak is obtained by using the time-frequency characteristics. The periodic step obtained using the frequency-domain characteristics is the initial value of the iteration. The maximum value and the next most considerable value are found in the step. The interval of the maximum value is used as the step of the next iteration until the average interval between the peak points obtained this time is the same as the last iteration, and the optimal peak point is obtained. K-mean clustering and Haar wavelet transform are used to locate the peak of the pulse wave. The lowest point of the pulse wave between the two peaks is the starting point of the pulse. The baseline drift curve is obtained by fitting the starting point with third-order spline interpolation. Finally, the denoising pulse wave can be obtained by subtracting the baseline drift curve from the pulse wave. Between the two starting points is a single-cycle pulse wave. Figure 5 (c) shows the signal after completing cycle division and removing baseline drift.

$$Y_i(x) = A_i + A_i(x - x_i) + C_i(x - x_i)^2 + D_i(x - x_i)^3, i = 0, 1, 2, 3, \ldots, 225. \tag{2.1}$$

The least squares method is used to fit the curves of three adjacent sampling points, where $x^{(i)}$ is the sampling point, A_i, B_i, C_i, D_i represent the constant coefficients in different orders, respectively.

Next, we sample the zero-mean normalization method and normalize the amplitude of the pulse wave.

$$Y^{(i)*} = \frac{Y - u}{\delta}, \delta^2 = \frac{1}{m}\sum_{i=1}^{m}(Y^{(i)} - u)^2, u = \frac{1}{m}\sum_{i=1}^{m} Y^{(i)} \tag{2.2}$$

FIGURE 2. (a) Multi channel pulse wave acquisition device. (b) A compound pressure sensor.

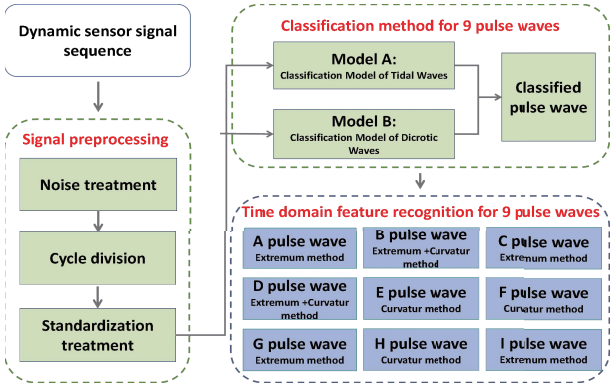

FIGURE 3. Data processing flow chart

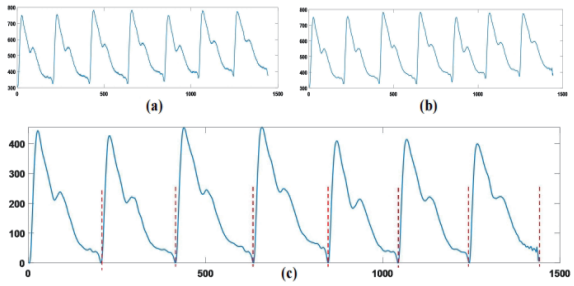

FIGURE 4. Acquire single cycle signal (a) Original pulse wave sequence (b) Signal after noise processing (c) Signal after completing cycle division and removing baseline drift

where $Y^{(i)}$ represents each sample, u represents the mean of all samples, δ represents the standard deviation of all samples, $Y^{(i)*}$ represents each normalized sample. The standardized single-cycle signals are manually labeled, the noise is labeled as 0, the pulse signal is labeled as 1, and the interference signal is labeled as 2.

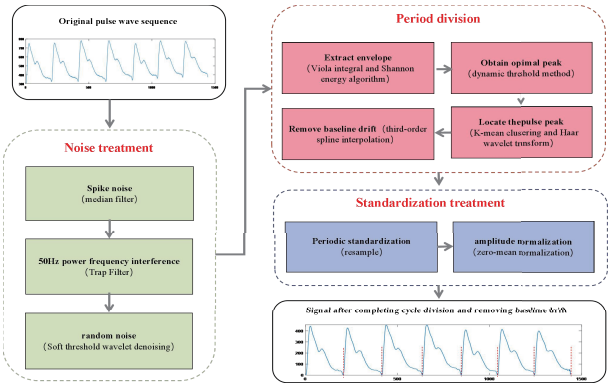

FIGURE 5. Signal Preprocessing Flowchart

2.2.2. *Pulse wave waveform classification based on CNN.* The 1D-DCNN model is shown in Figure 6 and includes an input layer, a convolutional layer (CONV), a fully connected layer (FC), and an output layer. The convolutional layer includes three operation steps: convolution, activation, and max pooling. Input one-dimensional single-cycle signal data, perform convolution operations on the input data, and use the sliding of convolution kernels to capture local patterns in the input data. The activation function introduces non-linear properties into the results of convolution operations, better fitting complex data patterns. To accelerate the learning speed of the model structure, max pooling downsamples the input representation by selecting the maximum value within the spatial region. After extracting the required overall features through multiple convolutional layer operations, flatten them into a feature tensor. The fully connected layer maps feature tensors to the output layer, learns the relationship between features and output results, and serves as a criterion for classification tasks, as shown in (2.3). This study divides the output results of heavy and TWs into three categories: extreme points, inflection points, and feature fusion.

$$y = g(kx + b). \tag{2.3}$$

Where, x is input, y represents output, k is weight, b is bias, and y isnon-linear activation. In the network, we need to train the weights and biases of CONV and FCs to enable the network to learn the complex functional expressions of input and output automatically. We need to set some hyperparameters and optimization methods of the 1D-DCNN model in advance to accelerate learning speed, as shown in Table 1. Based on experience, mini-batch processing accelerates gradient calculation and weight updates by placing multiple samples in one batch. We chose $64(2^8)$ as one batch. To dynamically adjust the learning rate, we use Adam as a gradient descent optimization algorithm based on past gradient information during the training process during the training process. As shown in (2.4)-(2.6), apply the Softmax function at the output layer of the model to convert the original value of the network's last layer into the probability distribution of the category so that the most likely category can be determined based on the probability size z_i.

$$z_i = \sum_j h_j W_{ji}, \tag{2.4}$$

$$softmax(z)_i = p_i = \frac{e^{z_i}}{\sum_{j=1}^{n} e^{z_i}}, \tag{2.5}$$

$$\hat{y} = \underset{i}{\text{argmax}} p_i. \tag{2.6}$$

The accuracy and training time of the 1D-DCNN for single-cycle waveform recognition were significantly influenced by sample size, model architecture, and hyperparameters. Given a limited dataset, optimization focused on adjusting the model architecture (number of convolutional layers, input/output channels) and hyperparameters (learning rate, input data length). Validation set performance guided the selection of the optimal configuration, minimizing training time. Experiments were conducted using Python 3.10.12, PyTorch 2.1.0 (with CUDA support), and an NVIDIA GTX 1660Ti GPU. The learning rate significantly impacts model convergence speed and stability. Eight learning rates, logarithmically spaced between 0.0001 and 0.01, were tested using gradient descent, stopping when average training loss fell below a threshold. Figure 7(a) shows validation set performance: accuracy increased and stabilized with higher learning rates, but training time grew exponentially (lower learning rates took longer). While larger learning rates yielded faster training, excessively high rates prevented convergence, ultimately increasing training time. A learning rate of 0.003 achieved optimal validation accuracy with relatively fast convergence. Subsequent training employed a learning rate scheduler, halving the initial 0.003 learning rate every 100 epochs. The number of convolutional layers determines the model's ability to learn increasingly abstract features. Figure 7(b) shows validation set performance using 2 to 8 convolutional layers. Accuracy initially increased with the number of layers but subsequently decreased while training time per epoch consistently increased. Adding layers doesn't guarantee linear performance improvement; excessive layers can lead to overfitting and slower training. With high validation accuracy and relatively fast convergence, optimal performance was achieved with six convolutional layers (CONV=6). The number of input and output channels in the convolutional layers affects the feature representation. Eight models, each with six convolutional layers and two fully connected layers, were designed with varying channel ratios (Table 2). The sixth convolutional layer consistently produced 32 feature tensors (size 4), concatenated into a 128-element vector for the fully connected layers. Figure 7 (c) shows validation set performance. Structures 1 and 2 exhibited superior accuracy; however, Structure 1, with fewer parameters, offered better computational efficiency and was therefore selected. To reduce the computational cost, the original 256-point signal was downsampled to 128, 64, and 32 points, corresponding to sampling frequencies of 112.5 Hz, 56.25 Hz, and 28.125 Hz, respectively. This avoided aliasing according to the Nyquist-Shannon sampling theorem. Figure 6 (d) shows validation accuracy for different input lengths; accuracy decreased below 128 points. Therefore, a 128-point single-cycle waveform was used. Training stopped after 30 consecutive epochs without improvement in the cross-entropy loss (2.7). Otherwise, backpropagation

and optimization continued.

$$\text{Loss} = -\sum_{i=0}^{c-1} y_i \log(p_i) = -\log(\ldots_{ic}). \tag{2.7}$$

Among them, $p = [p_0, \ldots, p_{c-1}]$ is a probability distribution, where each element is the probability that the sample belongs to class i. $y = [y_0, \ldots, y_{C-1}]$ is a unique hot code representation of the sample label when the sample belongs to a category. Otherwise, $y_i = 0$. C is the sample label. Based on the above experiment, we ultimately selected the CNN, which includes 6 CONV and 2 FC layers. The iteration stop condition is that the accuracy of the validation set does not decrease for 30 consecutive times, and the final classification result is output. The trend curves of the loss and accuracy of the training and validation sets during the training process are shown in Figure 8 (a)-(d), indicating that as the number of training rounds increases, the loss function gradually decreases while the accuracy gradually increases.

TABLE 1. Parameter Settings for CNN Models

Batch size	64
Kernel size	1×3
Pooling size	1×2
Stride	2
Loss function	Cross-Entropy Loss
Optimizer	Adam
Activation function	ReLU

TABLE 2. Different Structures of 1D-DCNN Model

			CONV (a-b)			FC (c-d)		
No.	Layer1	Layer2	Layer3	Layer4	Layer5	Layer6	Layer7	Layer8
1	1-2	2-4	4-8	8-16	16-32	32-32		
2	1-4	4-8	8-16	16-32	32-32	32-32		
3	1-4	4-16	16-32	32-32	32-32	32-32		
4	1-4	4-32	32-32	32-32	32-32	32-32	(128-64)	(64-3)
5	1-8	8-16	16-32	32-32	32-32	32-32		
6	1-8	8-32	32-32	32-32	32-32	32-32		
7	1-16	16-32	32-32	32-32	32-32	32-32		

2.2.3. *Time domain feature extraction methods for different types of pulse waves.* (1) Calculation method for extreme points of pulse waves Assuming the data length of a single cycle pulse wave $y(n)$ is N, the method to determine the i-th point as

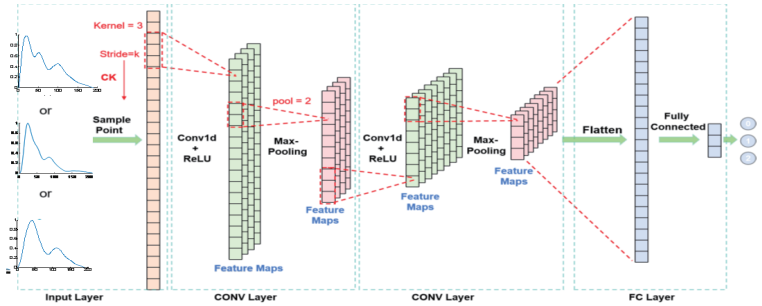

FIGURE 6. 1D-DCNN Model Structure

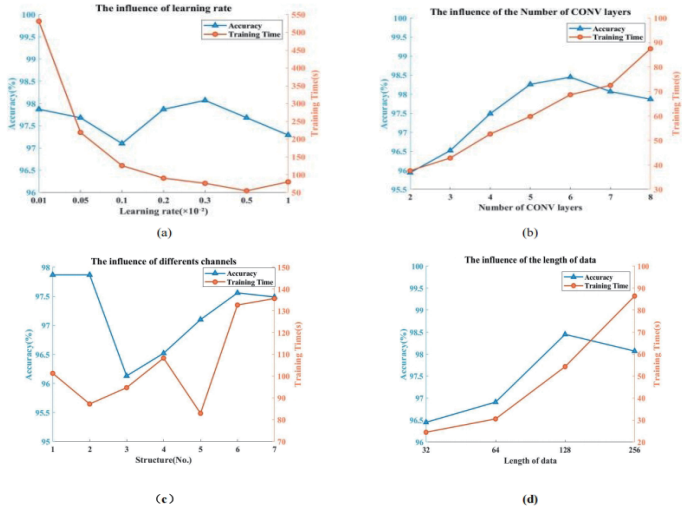

FIGURE 7. (a) Results of different learning rates on the validation set (b) Results of different convolutional layers on the validation set (c) Results of different input and output channels on the validation set (d) Results of different sampling points on the validation

the peak point is as follows:

$$\begin{cases} y(i) - y(i-1) > 0, \\ y(i) - y(i+1) > 0, \\ N > i > 1. \end{cases} \tag{2.8}$$

By traversing all sampling points on $y(n)$ and using the above formula, the position of the maximum pulse wave can be obtained:

$$\begin{cases} y(i) - y(i-1) < 0, \\ y(i) - y(i+1) < 0, \\ N > i > 1. \end{cases} \tag{2.9}$$

By traversing all sampling points on $y(n)$ and using the above for $+$, the position of the minimum pulse wave can be obtained.

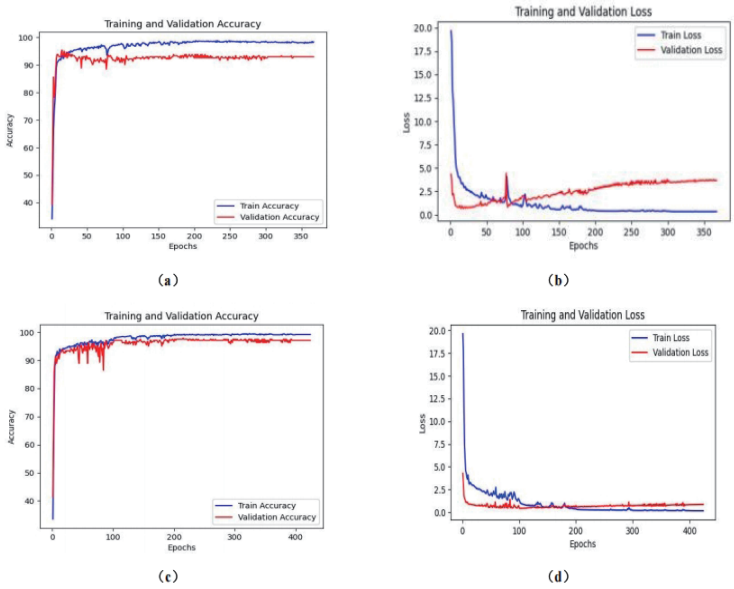

FIGURE 8. (a) Accuracy trend curves of tidal wave training set and validation set (b) Loss trend curves of tidal wave training set and validation set (c) Accuracy trends of the training and validation sets for dicrotic waves (d) Loss trends of the training and validation sets for dicrotic waves

(2) Calculation method of pulse wave inflection point Obtain the curvature transformation expression for $x(n)$ based on the definition of curvatur.

$$k(n) = \left(\frac{y_2}{1+y_1^2}\right)^{1.5}, n = 1, 2 \ldots N. \tag{2.10}$$

In the formula, y_1 is the first derivative of y and y_2 is the second derivative of y. In order to remove the interference term in the curvature, a 5-point smoothing filter is applied to the original curvature, and the number of filtering points is determined by the sampling frequency of the original data.

$$\begin{cases} k(i) - k(i-1) > 0, \\ k(i) - k(i+1) > 0, \\ N > i > 1. \end{cases} \tag{2.11}$$

By traversing all sampling points on $k(n)$ and using the above formula, the convex position of the pulse wave inflection point can be determined.

3. Algorithm verification

3.1. **Data sources.** The participants in this experiment are team members from our laboratory, including 86 males and 64 females, for a total of 150 participants. The volunteers of this experiment fully understood the experiment's content before the experiment and had the resources to participate in the experiment. The subject sample's specific inclusion criteria are shown as follows: (1) There is no skin disease

on the wrist; (2) The subject showed no significant upper limb tremors; (3) The subject does not have oblique pulse orno pulse. 1623 single-cycle waveforms were collected, including 537 TWs with extreme points, 559 with inflection points, and 527 disappearing pulse waves, respectively. The number of pulse waves with extreme points, inflection points, and disappearance is $641, 532, 450$, respectively.

3.2. **Evaluation results of pulse wave morphology classification model.**

3.2.1. *Performance evaluation of tidal wave three classification model.* As shown in Table 3 and Figure 7 (a), in the model validation set, the classification precision of the model extreme point is 93.59%, recall is 93.59%, $F1$ score is 93.59%, the classification precision of Inflection point is 95.45%, recall is 90.32%, $F1$ score is 92.82%, the classification precision of Fusion disappearance is 89.74%, recall is 95.89%, F1 score is 92.72%,the accuracy of the algorithm is 93.03%, the average precision is 92.93%, the average recall is 93.27%, the average F1 score is 93.04%, macro-F1 is 93.04%. It can be seen that the model performs well in training. It can be seen that the model performs well in prediction accuracy. As shown in Table 4 and Figure 7 (b), in the model test set, the classification precision of the model extreme point is 96.81%, recall is 96.81%, F 1 score is 96.81%, the classification precision of Inflection point is 94.59%, recall is 92.11%, $F1$ score is 93.33%, the classification precision of Fusion disappearance is 93.33%, recall is 95.89%, F1 score is 94.59%,the accuracy of the algorithm is 95.06%, the average precision is 94.91%, the average recall is 94.93%, the average F 1 -score is 94.91%, macro-F1 is 94.91%. It can be seen that the model performs well in training.

3.2.2. *Performance evaluation of the triple classification model for dicrotic wave.* As shown in Table 5 and Figure 8 (a), in the model validation set, the classification precision of the model extreme point is 95.00%, the recall is 97.44%, F1 score is 96.20%, the classification precision of Inflection point is 97.78%, recall is 94.62%, F1 score is 96.17%, the classification precision of Fusion disappearance is 98.65%, recall is 100.00%, $F1$ score is 99.32%,the accuracy of the algorithm is 97.13%, the average precision is 97.14%, the average recall is 97.35%, the average F 1 score is 97.23%, macro-F1 is 97.23%. It can be seen that the model performs well in training. The model performs well in prediction accuracy. As shown in Table 6 and Figure 8 (b), in the model test set, the classification precision of the model extreme point is 97.78%, recall is 93.62%, $F1$ score is 95.65%, the classification precision of Inflection point is 92.11%, recall is 92.11%, $F1$ score is 92.11%, the classification precision of Fusion disappearance is 90.91%, recall is 95.89%, F1 score is 93.33%,the accuracy of the algorithm is 93.70%, the average precision is 93.60%, the average recall is 93.87%, the average F 1 -score is 93.70%, macro-F1 is 93.70%. It can be seen that the model performs well in training.

3.2.3. *Evaluation of time-domain feature extraction algorithms for pulse waves.* As the purpose of this study is to predict specific eigenvalues that belong to regression problems, Adjusted R-Square($R^2_{ajusted}$) Mean Absolute Error (MAE) Root Mean Square Error (RMSE) are usually used to evaluate the training accuracy of the model Randomly select 100 extreme points, inflection points, and fused disappearance pulse waves from TWs and DWs to evaluate the recognition results of DW

and TW coordinate points. For the convenience of evaluation, this paper evaluates the algorithm's accuracy by calculating the results of the three TW and DW states.The results in Table 6 show that after using the algorithm for classification and recognition in this study, the lowest correction regression coefficient for the three characteristics of pulse wave time-domain TW is 0.97, and the lowest correction coefficient for DW is 0.96. The corresponding statistical parameter values for each feature point dataset, such as and are less than 2, indicate that the algorithm model has achieved high accuracy in feature point recognition.

As shown in Table 7, using traditional methods to identify feature points on the same test set data, it was found that the correction coefficient reached 0.92 only when the TWs were extreme points and the statistical parameters were all below 5.However, the recognition correction coefficients for other feature points are all negative, and the statistical parameter values are relatively large. When the TW and DW are Infection and Fusion disappearance, the RMSE values reach $312.79, 501.64, 522.85, 613.41$, indicating that the predicted feature point positions differ significantly from the actual ones. The reason for the low recognition accuracy of the traditional curvature method is that the pulse waveform is complex, and there is interference, so the algorithm's robustness could be better. The recognition is higher when TWs and DWs are extreme points, which is not significantly different from the algorithm proposed in this paper.

TABLE 3. Valid Dataset Results of Tidal Wave Three Classification Model

Valid Dataset				
Index(%)	extreme poin	Inflection point	Fusion disappearance	Average
Precision(%)	96.81	94.59	93.33	94.91
Recall(%)	96.81	92.11	95.89	94.93
F1-score(%)	96.81	93.33	94.59	94.91
Accuracy(%)		95.06		
macro-F1(%)		94.91		

TABLE 4. Test Set Results of Tidal Wave Three Classification Mode

Test Dataset				
Index	extreme poin	Inflection point	Fusion disappearance	Average
Precision(%)	93.59	95.45	89.74	92.93
Recall(%)	93.59	90.32	95.89	93.27
F1-score(%)	93.59	92.82	92.72	93.04
Accuracy(%)		93.09		
macro-F1(%)		93.04		

TABLE 5. Valid Dataset Results of of the triple classification model for dicrotic waves

Valid Dataset				
Index(%)	extreme poin	Inflection point	Fusion disappearance	Average
Precision(%)	95.00	97.78	98.65	97.14
Recall(%)	97.44	94.62	100.00	97.35
F1-score(%)	96.20	96.17	99.32	97.23
Accuracy(%)		97.13		
macro-F1(%)		97.23		

TABLE 6. Test Set Results of the triple classification model for dicrotic waves

Test Dataset				
Index	extreme poin	Inflection point	Fusion disappearance	Average
Precision(%)	97.78	92.11	90.91	93.60
Recall(%)	93.62	92.11	95.89	93.87
F1-score(%)	95.65	92.11	93.33	93.70
Accuracy(%)		93.70		
macro-F1(%)		93.70		

TABLE 7. Effect of dicrotic Wave and Tidal Wave Coordinate Point Recognition

		Tidal wave			Dicrotic wave		
Methods	Results	extreme point	Inflection point	Fusion disappearance	extreme point	Inflection point	Fusion disappearance
This article's algorithm	R	0.98	0.97	0.99	0.98	0.96	0.98
	MAE	0.31	0.75	0.21	0.45	0.84	0.25
	RSME	0.52	1.34	0.13	0.67	1.45	0.23
Traditional method	R	0.92	-0.82	-10.57	0.90	-0.65	-14.69
	MAE	0.37	11.05	8.64	0.35	14.22	15.48
	RSME	1.58	312.79	501.64	2.64	522.85	613.41

4. CONCLUSION

Starting from hemodynamics, this study analyzes the formation mechanism of pulse waves and determines the morphology of heavy and TWs. On this basis, a pulse wave time-domain feature extraction algorithm based on morphological features was proposed. Firstly, deep learning algorithms are used to identify the three states of pulse waves and TWs. Then, the curvature and extremum methods are combined to achieve parameter recognition of the time-domain characteristics of pulse waves. Experiments have shown that the algorithm has high recognition accuracy and is widely used. Its accuracy and directness make it valuable for clinical applications like noninvasive blood pressure and central pulse pressure measurement and the quantification of pulse wave characteristics (e.g. Karterial reflection

wave enhancement index). This significantly improves vascular disease prevention, diagnosis, treatment, and prognosis.

5. Author contributions

Yitao Zhang and Hao Wang designed the study, and served as co corresponding authors.Yang Li and Xingguang Geng performed the experiments and analysis,and had the same contribution, therefore they are both the first authors. Yao Fei and Xiaoyu Wang wrote the paper and took care of figures, tables and other graphical and statistical aspects. All authors read and approved the final manuscript.

6. Data Availability Statement

The raw/processed data required to reproduce these findings cannot be shared at this time as the data also forms part of an ongoing study.

References

[1] C. Y. Chang, X. Luo, B. Y. Liao, *A study of pulse waves and the method of function combination and approximation*, Journal of Applied Sciences **2** (2000), 135–138.

[2] X. F. Chen, *Research on Pulse Wave Feature Extraction Algorithm and Its Application*, Dalian University of Technology, 2006.

[3] X. R. Ding, N. Zhao and G. Z. Yang, *Continuous blood pressure measurement from invasive to unobtrusive: Celebration of 200th birth anniversary of Carl Ludwig*, IEEE Journal of Biomedical and Health Informatics **20** (2016), 1455–1465.

[4] C. Guo, Z. Jiang, H. He, Y. Liao and D. Zhang, *Wrist pulse signal acquisition and analysis for disease diagnosis: A review*, Computers in Biology and Medicine **143** (2022): 105312.

[5] J. N. Hou, Y. T. Zhang, S. L. Zhang, X. G. Geng, J. Zhang, C. L. Chen and H. Y. Zhang, *A novel angle extremum maximum method for recognition of pulse wave feature points*, Computer Methods and Programs in Biomedicine **189** (2020): 103521.

[6] X. J. Huang, W. Xing and F. Li, *Research on pulse wave feature information based on syntactic pattern recognition*, Chinese Journal of Medical Devices **29** (2005), 325–327.

[7] J. Jin, X. G. Geng, Y. T. Zhang, H. Y. Zhang and T. C. Ye, *Pulse wave analysis method of cardiovascular parameters extraction for health monitoring*, International Journal of Environmental Research and Public Health **20** (2023): 2597.

[8] J. Q. Li, R. Li, Z. Z. Chen, G. Q. Deng, H. Wang, C. X. Mavromoustakis, H. Song and Z. Ming, *Design of a continuous blood pressure measurement system based on pulse wave and ECG signals*, IEEE Journal of Translational Engineering in Health and Medicine **6** (2018), 1–14.

[9] Q. Li and G. D. Clifford, *Dynamic time warping and machine learning for signal quality assessment of pulsatile signals*, Physiological Measurement **33** (2012), 1491–1504.

[10] J. Z. Liu, *Research on pulse porter eigenpoint recognition based on waveform features and wavelet*, Journal of Instruments and Meters **37** (2016), 376–386.

[11] W. Liu, X. Fang, Q. Chen, Y. Li and T. Li, *Reliability analysis of an integrated device of ECG, PPG and pressure pulse wave for cardiovascular disease*, Microelectronics Reliability **87** (2018), 183–187.

[12] R. Mukkamala, G. S. Stergiou and A. P. Avolio, *Cuffless blood pressure measurement*, Annual Review of Biomedical Engineering **24** (2022), 203–230.

[13] T. Panula, J. P. Sirkia, D. Wong and M. Kaisti, *Advances in non-invasive blood pressure measurement techniques*, IEEE Reviews in Biomedical Engineering **16** (2022), 424–438.

[14] S. Rastegar and H.Gholamhosseini, *Non-invasive continuous blood pressure monitoring systems: current and proposed technology issues and challenges*, Physical and Engineering Sciences in Medicine **43** (2020),11–28.

[15] R. Shriram, A. Wakankar, N. Daimiwal and D. Ramdasi, *Continuous cuffless blood pressure monitoring based on PTT*, in: Proceedings 2010 International Conference on Bioinformatics and Biomedical Technology, IEEE, 2010, pp. 51–55.
[16] W. Sun, N. Tang and G. P. Jiang, *Research on feature point recognition and preprocessing methods for pulse wave signals*, Journal of Biomedical Engineering **32** (2015), 197–200.
[17] G. T. Wang, X. G. Geng and L. Huang, *Multi-morphological pulse signal feature point recognition based on one-dimensional deep convolutional neural network*, Information **14** (2023): 70.
[18] G. T. Wang, Y. T. Zhang, X. G. Geng, X. X. Kang, J. Zhang, H. Y. Zhang, M. R. Wang, X. J. Wang and Q. Y. Li, *A method for assessing human health status based on pulse waves*, Journal of Nonlinear and Convex Analysis **24** (2023), 1561–1579.
[19] S. Wei, T. Ning, G. P. Jiang, *Research on feature point recognition and preprocessing methods for pulse wave signals*, Journal of Biomedical Engineering **32** (2015), 197–201.
[20] J. J. Yan, X. L. Cai, G. Y. Zhu, R. Gu H. X. Yan and Y. Q. Wang, *A non-invasive blood pressure prediction method based on pulse wave feature fusion*, Biomedical Signal Processing and Control **74** (2022): 103523.
[21] M. L. Zhang, L. J. Xu and W. F. Huang, *Pulse wave feature extraction based on improved slop thresholding method*, Electronic Measurement Technology **40** (2017), 96–99.

Manuscript received September 11, 2024
revised December 20, 2024

Y. Li
Department of Stomatology, Beijing Tiantan Hospital, Capital Medical University, Beijing, China
E-mail address: 13381278293@163.com

X. Geng
Institute of Microelectronics of Chinese Academy of Sciences, Beijing, China
E-mail address: gengxingguang@ime.ac.cn

F. Yao
Institute of Microelectronics of Chinese Academy of Sciences, Beijing, China
E-mail address: yaofei@ime.ac.cn

X. Wang
Department of Stomatology, Beijing Tiantan Hospital, Capital Medical University, Beijing, China
E-mail address: 13701131933@139.com

Y. Zhang
Institute of Microelectronics of Chinese Academy of Sciences, Beijing, China
E-mail address: zhangyitao@ime.ac.cn

X. Wang
Department of Stomatology, Beijing Tiantan Hospital, Capital Medical University, Beijing, China
E-mail address: wang@hotmail.com

Hua Hua
Sichuan Institute for Translational Chinese Medicine, Sichuan, China:
Sichuan Academy of Chinese Medicine Sciences, Sichuan, China
E-mail address: hrhr2014@163.com